

Irrigation Signals Detected from SMAP Soil Moisture Retrievals

Patricia M. Lawston^{1,2}, Joseph A. Santanello, Jr.², Sujay V. Kumar²

¹Earth System Science Interdisciplinary Center, University of Maryland, College Park, Maryland, USA.

²Hydrological Sciences Laboratory, NASA Goddard Space Flight Center, Greenbelt, Maryland, USA.

Corresponding author: Patricia Lawston (patricia.m.lawston@nasa.gov)

Key Points:

- To date, irrigation detection from passive microwave satellites has proven difficult even over well-known, expansive regions of agriculture
- The new, enhanced soil moisture product from the Soil Moisture Active Passive satellite can detect irrigation signals in three regions
- Satellite detection of irrigation increases our ability to understand, monitor, and predict human impacts on the water cycle.

18 **Abstract**

19 Irrigation can influence weather and climate, but the magnitude, timing, and spatial extent of
20 irrigation are poorly represented in models, as are the resulting impacts of irrigation on the
21 coupled land-atmosphere system. One way to improve irrigation representation in models is to
22 assimilate soil moisture observations that reflect an irrigation signal to improve model states.
23 Satellite remote sensing is a promising avenue for obtaining these needed observations on a
24 routine basis, but to date, irrigation detection in passive microwave satellites has proven difficult.
25 In this study, results show that the new Enhanced soil moisture product from the Soil Moisture
26 Active Passive (SMAP) satellite is able to capture irrigation signals over three semi-arid regions
27 in the western United States. This marks an advancement in earth-observing satellite skill and the
28 ability to monitor human impacts on the water cycle.

29

30 **Plain Language Summary**

31 When farmers use irrigation over large areas, it can make the air cooler and more humid;
32 sometimes even changing how clouds form and where rain falls. For this reason, it's important to
33 know where and when irrigation is used, how wet the soil becomes, and how long it stays
34 artificially wet. This information is critical for improving weather models, and therefore
35 forecasts, in the food baskets of the world. However, until now it has been difficult to find
36 accurate and consistent irrigation practice information over time and for large areas. In this
37 paper, we show that a NASA satellite which measures soil moisture routinely across the globe is
38 able to detect wet soil resulting from irrigation in naturally dry environments. This marks an
39 advancement in earth-observing satellite skill and improves our ability to monitor and predict
40 human impacts on the water cycle.

41 **1 Introduction**

42 Irrigation is required to meet the world's food demands, but also drastically alters the
43 water cycle. By increasing soil moisture (SM), irrigation repartitions the surface energy balance,
44 increasing evaporation and decreasing sensible heat flux and temperature (Kanamaru &
45 Kanamitsu, 2008; Bonfils & Lobell, 2007). The altered energy balance can be significant enough
46 to influence clouds and precipitation through land-atmosphere interactions driven by planetary
47 boundary layer feedbacks (Kueppers & Snyder, 2011; Qian et al., 2013; Lawston et al., 2015).
48 Thus, irrigation has shown the potential to impact the atmosphere from local to climate scales
49 and is increasingly recognized as an important process for representation in weather and climate
50 models (Sorooshian et al. 2011; Alter et al. 2015; Puma and Cook, 2010; among others).

51 Two main avenues exist for incorporating irrigation into weather models: 1) irrigation
52 parameterizations, and 2) data assimilation (DA) of surface observations. Irrigation modules
53 have grown in complexity (Ozdogan et al. 2010; Evans and Zaitchik, 2010; Leng et al. 2014;
54 Pokhrel et al., 2016), but consistent irrigation practice and SM data are needed globally to
55 evaluate and improve these parameterizations (Lawston et al., 2017). DA avoids the need for
56 assumptions of human practices, but the SM observations must be skillful enough to represent
57 the irrigation signals (Kumar et al. 2015). Thus, to fully leverage either of these avenues requires
58 SM observations with high enough spatial and temporal resolution to distinguish differences
59 between irrigated and non-irrigated areas.

60 Satellite remote sensing of SM is a natural choice to address this need, but to date it has
61 been difficult to detect irrigation in passive SM retrievals. Kumar et al. (2015) showed the
62 Advanced Scatterometer (ASCAT), the Advanced Microwave Scanning Radiometer 2
63 (AMSR2), and the Soil Moisture Ocean Salinity (SMOS) were unable to identify seasonal
64 features of irrigation in the California Central Valley, and showed limited skill at best in
65 Nebraska. The most recent SM mission, NASA's Soil Moisture Active Passive (SMAP), has
66 shown improved information content as compared to previous SM satellites (Kumar et al. 2017),
67 raising interest in whether SMAP also shows improvement in irrigation detection. In this study,
68 we explore the utility of SMAP SM retrievals for identifying irrigated regions and timing. While
69 other satellite-based irrigation detection methods exist (e.g., optical/thermal infrared, Thenkabail
70 et al., 2009), the ~two-day return time of SMAP and the ability to directly monitor SM
71 conditions could offer a distinct and advantageous approach for obtaining routine irrigation
72 information.

73 **2 Data and Methods**

74 **2.1 Data**

75 The SMAP satellite, launched in January 2015, contains a L-band passive microwave
76 radiometer and uses a single channel retrieval algorithm to provide near surface (i.e., 0-5cm) SM
77 globally, every 1-3 days at 36 km resolution (Entekhabi et al., 2010). SMAP validation studies
78 show that the accuracy of the SM products meets mission requirements (<4%; Colliander et al.,
79 2017) and that SMAP can be used to assess hydrologic processes, such as SM drydowns
80 (Shellito et al., 2016; McColl et al., 2017). The SMAP Level 3 Enhanced SM dataset, used in
81 this study, exploits the oversampling of the antenna overpasses to enhance the spatial resolution
82 of the SM retrievals, posted on a 9 km grid (O'Neill et al., 2016). The analysis focuses on 2016,
83 the only full year available of the Enhanced dataset.

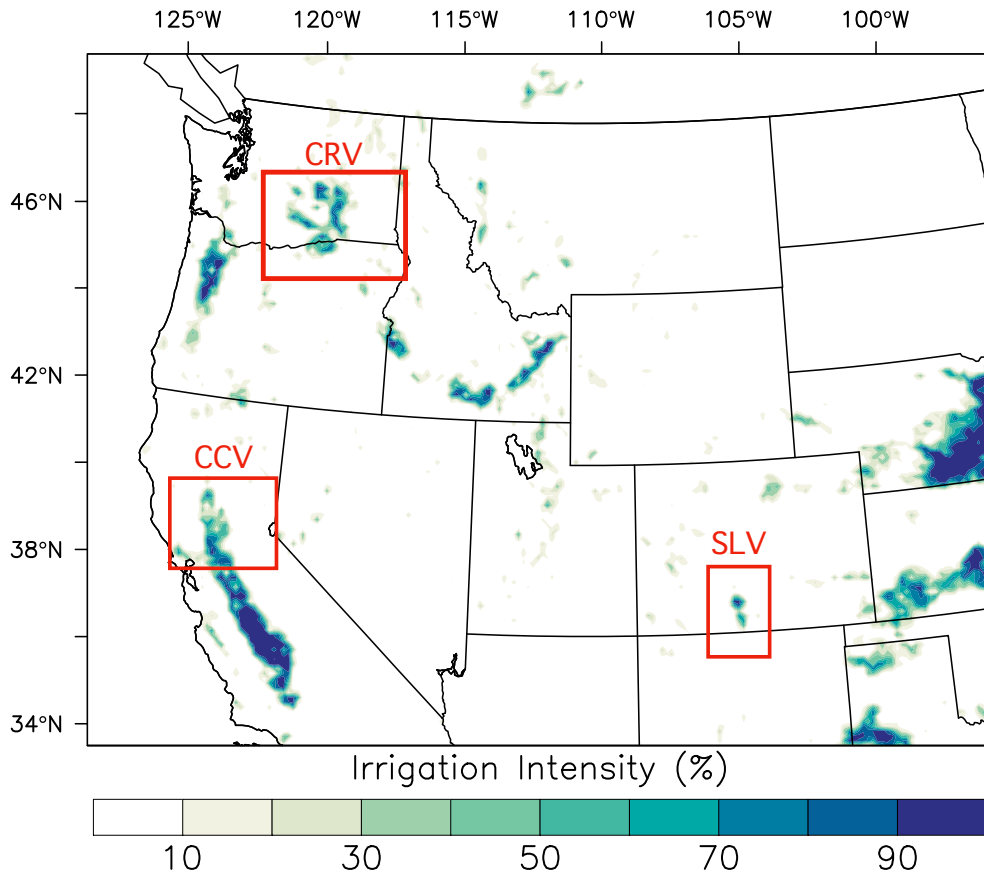
84 As SM is likely to deviate from the precipitation signal during irrigation periods, Stage
85 IV quantitative precipitation estimates from the National Center for Environmental Prediction
86 are analyzed together with SM. These estimates are derived from radar and rain gauges and
87 gridded at 4 km resolution. Additional in-situ precipitation data are used from the California
88 Irrigation Management Information System (CIMIS) and the Community Collaborative Rain,
89 Hail, & Snow (CoCoRaHS) network.

90 Datasets used to infer local agricultural practices are the Crop Progress and Condition
91 Bulletins from United States Department of Agriculture National Agricultural Statistical Service
92 (USDA NASS, 2016) and the Terra True Color Reflectance image dataset from Moderate
93 Resolution Imaging Spectroradiometer (MODIS). The crop bulletins are useful for assessing
94 planting, harvest, and growth conditions, while the MODIS images offer a detailed view of the
95 changing landscape that can corroborate the timing of crop growth and harvest.

96 **2.2 Methods**

97 The aforementioned datasets are analyzed for three regions in the western United States,
98 known to contain a range of irrigated agriculture (Figure 1). The Sacramento Valley in northern
99 California, the San Luis Valley in southern Colorado, and the Columbia River Valley in
100 southeastern Washington are semi-arid regions and receive the majority of their precipitation in
101 winter. Thus, warm season irrigation is required to cultivate crops, creating a stark contrast in

102 vegetation, and presumably SM, between the irrigated agriculture and surrounding precipitation-
103 deficient area. These three regions are chosen to explore the outcome of differing irrigation
104 practices, spatial extent, and other complicating factors on the detection from SMAP.



105

106 Figure 1. Three case study regions: the Sacramento Valley (CCV), California; San Luis Valley
107 (SLV), Colorado; Columbia River Valley (CRV), Washington, overlaid on percent of areas
108 equipped for irrigation (Salmon et al. 2015).

109 For each region, the sensitivity of SMAP SM retrievals to irrigation is analyzed as
110 follows: 1) spatially for selected dates during and outside of the growing season, 2) temporally at
111 irrigated and non-irrigated points over a full year, and 3) by using a regional, time-integrated and
112 normalized metric of SM and precipitation to assess the bulk signal in mid-summer. This third
113 metric is calculated by summing the SMAP SM retrievals over June and July 2016 and then
114 normalizing by the minimum and maximum for each study area and time period (hereafter
115 ‘integrated SM’). Only days in which SMAP provides full coverage of each study area are used.
116 The same calculations are completed using the Stage IV gridded precipitation to obtain the time-
117 integrated, normalized precipitation (hereafter, ‘integrated rainfall’). The resulting maps allow
118 for quick identification of the wettest areas in terms of SM and those that received the greatest
119 rainfall in each region. Assuming relatively similar surface and soil properties and topography,
120 consistently high SM corresponding with relatively low precipitation over the growing season
121 can be used as an indicator of irrigation. All three analyses were completed for each study area,

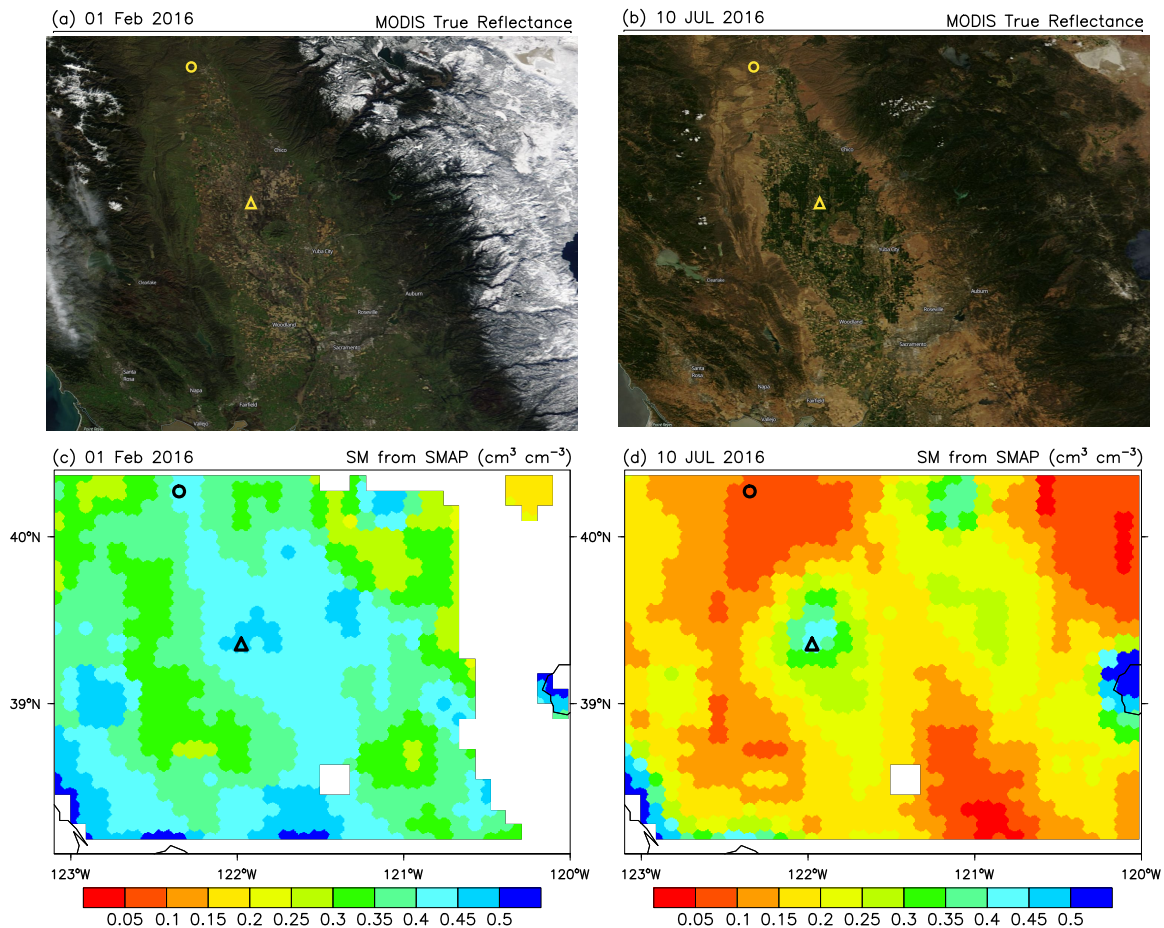
122 but for brevity, only the complete set of analyses is shown for the first case study. The remaining
123 analyses are included in the supplement.

124 **3 Results**

125 3.1 Sacramento Valley

126 The Sacramento Valley, in the northern California Central Valley (CCV), produces 95%
127 of California's rice (CA Rice, 2017). Each year, the fields are flooded and aurally seeded in late
128 April through early May. The water level is sustained throughout the season and then drained
129 shortly before maturity, typically in August. Harvest begins in September and concludes in
130 November (CA Rice, 2017).

131 Figure 2 shows the significant change in landscape appearance from Terra imagery on
132 February 1, during the wet season, as compared to July 10, during the dry season. The greenness
133 over the region present in February turns brown by July, with the exception of only the irrigated
134 rice and higher elevation forests. SMAP SM retrievals identify these contrasts as February is
135 uniformly wet ($> 0.30 \text{ cm}^3/\text{cm}^3$) and July is dry except for the irrigated valley and forest, which
136 show much higher SM. This figure implies that SMAP is realistically sensing seasonal SM
137 characteristics and that SM is elevated in the irrigated valley.

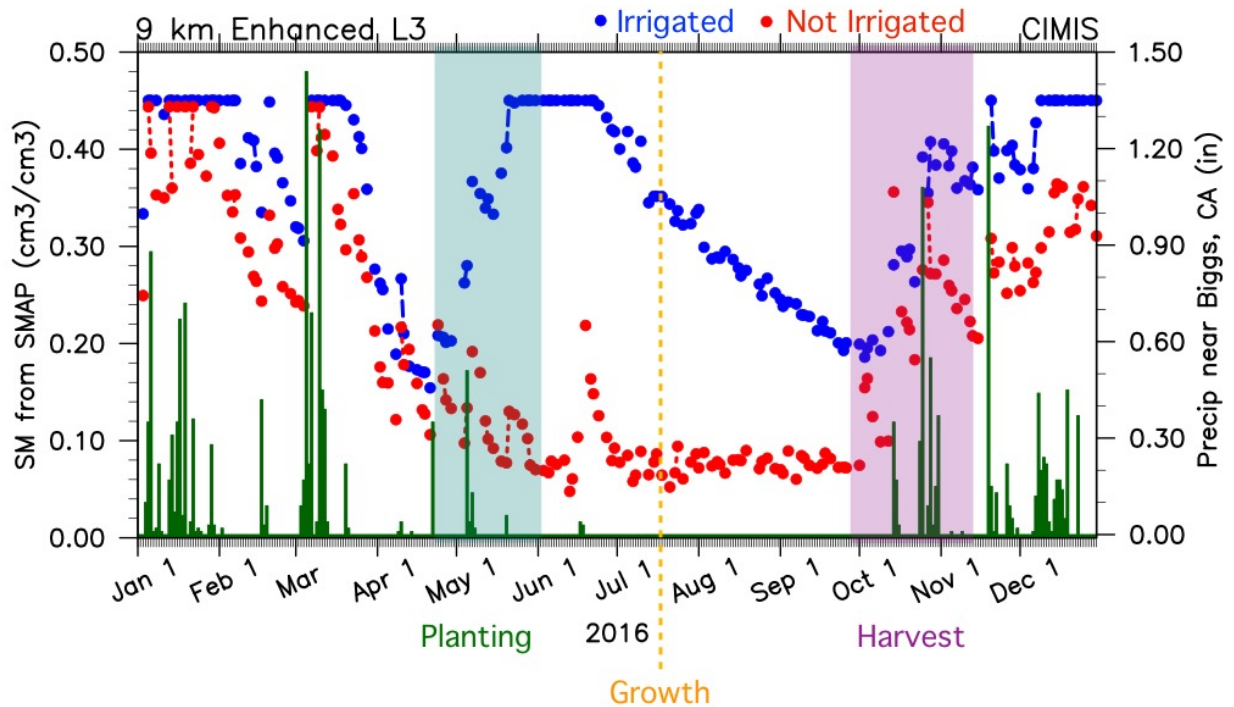


138

139 Figure 2. MODIS Terra true color reflectance for (a) February 1, 2016 and (b) July 10, 2016.
 140 SMAP Level 3 Enhanced SM (cm^3/cm^3) for (c) February 1, 2016 and (d) July 10, 2016. Triangle
 141 and circle markers indicate the irrigated and non-irrigated sites, respectively.

142 An irrigated and a non-irrigated site (Fig. 2) are chosen for further analysis of temporal
 143 characteristics. Figure 3 shows SMAP SM at each of these sites (left axis), along with daily
 144 precipitation (right axis) from the Biggs CIMIS site. At both sites, SM is high November through
 145 March (i.e., 0.3 to 0.45 cm^3/cm^3), then gradually decreases from mid-March into April with the
 146 transition to the dry season. The sites behave similarly as they respond to widespread
 147 precipitation during the wet season. However, the sites abruptly diverge in May, exhibiting
 148 markedly different behavior for the rest of the growing season. The non-irrigated site dries down
 149 through May, responding to a few, small rainfall events. In contrast, SM at the irrigated site
 150 increases dramatically in May reaching and sustaining saturation from mid-May to mid-June.
 151 The timing is consistent with the USDA NASS crop reports that show planting of rice, which
 152 includes flood irrigation, in late April through May. During this time, the SM signal is in direct
 153 opposition to the rainfall (i.e., decreasing intensity, frequency), suggesting that the SM signal is
 154 in fact responding to the onset of flood irrigation.

155

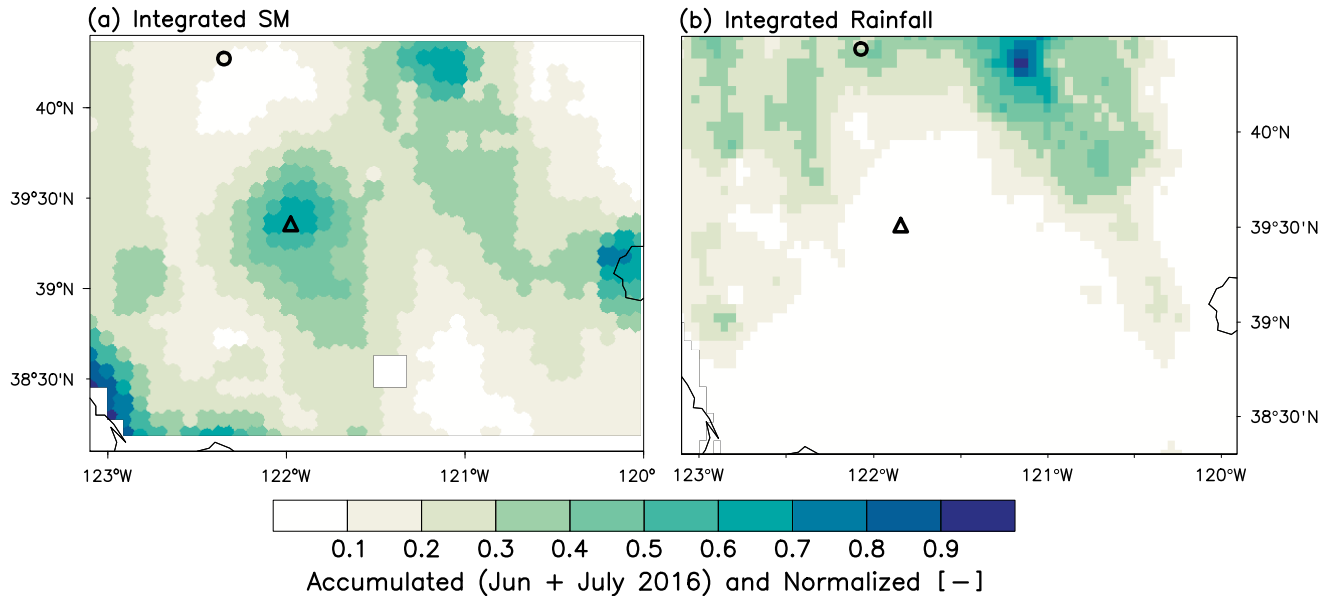


157

158 Figure 3. SMAP SM at the irrigated site (blue) as compared to the non-irrigated site (red) in the
 159 CCV. Right axis shows daily precipitation from the Biggs CIMIS site. Planting, growth, and
 160 harvest windows are from USDA NASS reports.

161 Beginning late in June, SM at the irrigated site steadily decreases until rain returns in
 162 October. The SMAP-sensed dry-down is likely a result of two factors. First, the crop report notes
 163 that in early July the rice has begun to “break out” of the water (i.e., “growth” in Fig. 3). This
 164 means the landscape SMAP senses has transitioned from essentially open water to water
 165 underneath vegetation, which increasingly attenuates the moisture signal with growth. Second,
 166 late in the summer the fields are drained before crop maturity and fall harvest (CA Rice, 2017).
 167 The harvest and growth periods are thus consistent with what is seen in the gradual decline of
 168 SMAP SM over the summer period.

169 Figure 4 shows the integrated SM and rainfall metric maps. As in the 14 July SM
 170 retrievals, the irrigated valley stands out as one of the wettest locations in the region, on par with
 171 the bordering mountains east of the Valley. The integrated rainfall shows that the precipitation
 172 falls along the higher elevations, wrapping around the valley. The irrigated valley is one of the
 173 wettest spots in the region in terms of SM, despite relatively little rainfall. Collectively, these
 174 analyses demonstrate that SMAP is able to identify the spatial signature and seasonal timing of
 175 irrigation in the Sacramento Valley.



176

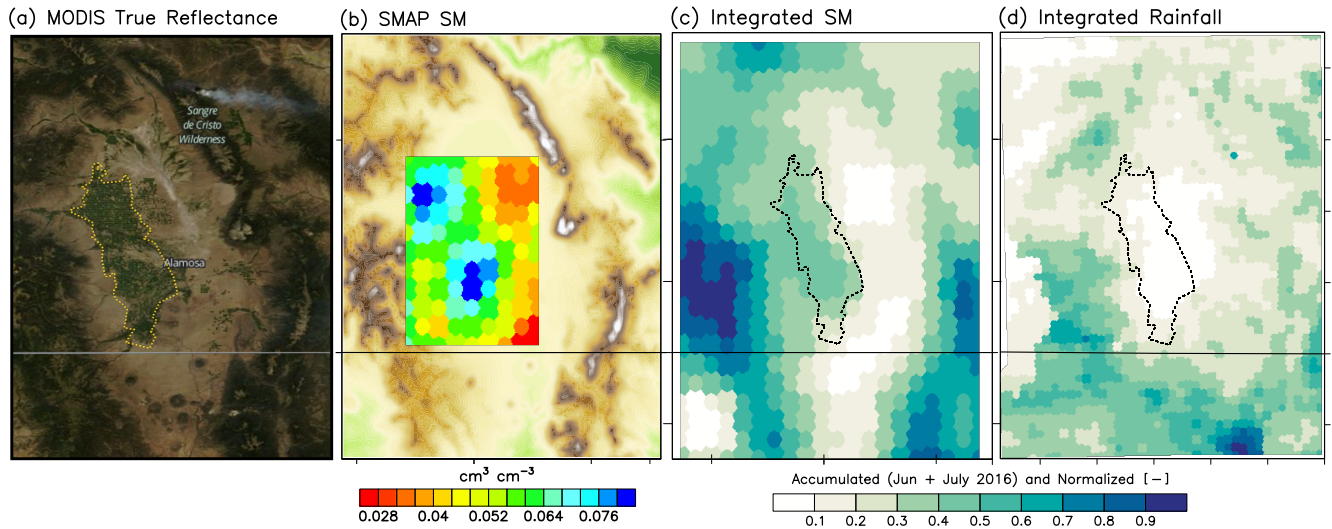
177 Figure 4. Time-integrated (June 1 to July 31) and normalized (a) SM and (b) precipitation.
 178 Markers as in Fig. 2.

179 3.2 San Luis Valley

180 The San Luis Valley (SLV) sits at an elevation over 2300 meters, nestled in between the
 181 San Juan and Sangre de Cristo mountains. Snow melt is the main source of irrigation water,
 182 through both surface water and aquifer recharge. Irrigation is clustered on the western side of the
 183 valley, where center pivot sprinklers irrigate predominately potatoes, alfalfa, and barley (USDA,
 184 2017).

185 Figure 5b shows SMAP SM on 14 July 2016, masked out for all locations except the
 186 valley. The magnitude of SM is low, but the irrigated region stands out as being wetter
 187 (i.e., $0.025 \text{ cm}^3/\text{cm}^3$) than the surrounding area. This includes two local SM maxima apparent
 188 only during the growing season (S2). As in the CCV, the precipitation is confined mostly to the
 189 ridge tops and the integrated metrics show relatively high SM in June and July in the irrigated
 190 valley, despite little rainfall (Fig. 5c,d). This suggests that the relative SM and precipitation
 191 metric supports and is consistent with the onset and spatial extent of irrigation in this region.

192 It should be noted that the time series analyses of irrigated and non-irrigated areas (S2)
 193 are not as clear as in the CCV. A shift in trend is evident, whereby the irrigated area is often
 194 wetter in the growing season and the reverse is true in the off-season. However, these differences
 195 are small and within the range of instrument error ($0.04 \text{ cm}^3/\text{cm}^3$), limiting robust conclusions
 196 from the time series analysis alone. These issues exhibit the difficulty of sensing a small area of
 197 irrigation closely bounded by complex topography.



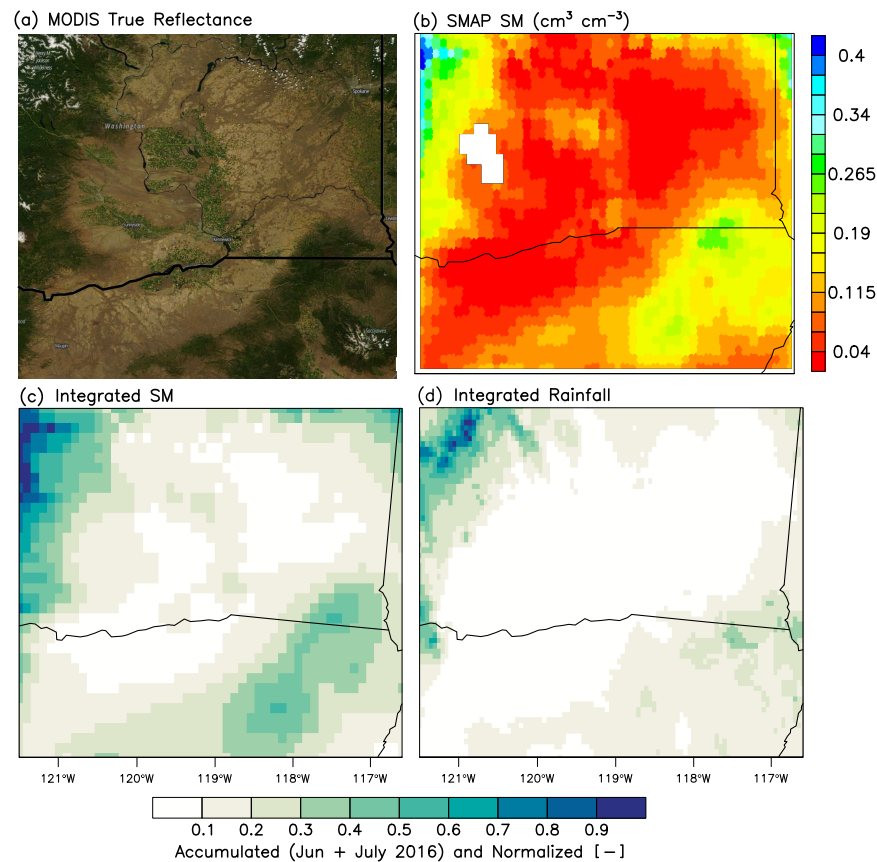
198

199 Figure 5. (a) MODIS Terra image of the SLV; irrigated valley outlined in yellow. (b) SMAP SM
 200 retrievals on 14 July 2016 overlaid on a topography. Time-integrated and normalized (c) SM and
 201 (d) rainfall; irrigated valley outlined in black.

202 **3.3 Columbia River Valley**

203 The third study region, referred to as the Columbia River Valley (CRV) for simplicity, is
 204 actually centered on the convergence of three major rivers: the Columbia, the Snake, and the
 205 Yakima. As these rivers are the primary source of irrigation water for eastern Washington, the
 206 agriculture clings to the rivers and lowest elevations, creating a distinct pattern of greenness (Fig.
 207 6a). In contrast to the other regions, a greater variety of crops are cultivated, including apples,
 208 grapes, hops, among others (USDA, 2017). Drip irrigation has grown in popularity here, but
 209 sprinkler and flood methods are still most common (USDA, 2013).

210 The spatial comparison of SM during and outside of the growing season, exhibits
 211 elevated SM in July in areas of irrigation as compared to February, indicating that the irrigation
 212 timing is again captured spatially (S3). Figure 6 (c, d), shows the integrated SM and rainfall
 213 maps. As in the previous cases, rainfall is generally confined to the higher elevations creating a
 214 rain-shadow and precipitation minimum for the valley in June and July. However, the integrated
 215 SM shows elevated SM in the locations of the irrigated agriculture. Even more convincingly, the
 216 shape of the elevated SM resembles the geography of the agriculture.



218

219 Figure 6. (a) Terra image of the CRV. (b) SMAP SM for 15 July 2016. Time-integrated and
 220 normalized (c) SM and (d) rainfall.

221 A complicating factor in this region is the irrigation's proximity to the large river systems
 222 and several lakes. Water bodies within the SMAP field of view could contaminate (i.e.
 223 incorrectly increase) the land SM near the rivers. This proves problematic, not only in the spatial
 224 plots, but also in defining appropriate locations for the time series analysis (S3). As in the SLV,
 225 there is a shift evident between the growing and off-season, but it is unclear to what extent the
 226 nearby water bodies, rather than the irrigated agriculture alone, contribute to this difference.

227 4 Discussion

228 The CCV was an ideal region for irrigation detection due to the consistent, extensive
 229 flood irrigation, ancillary observations, and rain-free summer. Flood irrigation proved the easiest
 230 method to detect, while comparatively water-conservative sprinkler irrigation in the SLV and
 231 CRV created subtler SM contrasts. The size of the irrigated area is also factor in detection.
 232 Although a 36x36km uniformly irrigated region could theoretically be captured by a perfectly
 233 aligned overpass, the likelihood of SMAP responding primarily to irrigation increases with the
 234 size of the irrigated area. The scale of irrigation at SLV is likely close to a practical minimum

235 required for SMAP-based detection based on these methods and results. In all three case studies,
236 despite differences in irrigation scale and methods, the bulk, seasonal timing of irrigation was
237 apparent in the spatial plots and integrated metrics.

238 The semi-arid, Mediterranean climate in these regions necessitates irrigation and creates
239 the contrast between the irrigated and surrounding land. The same methods were applied to
240 eastern Nebraska, where sprinkler irrigation is abundant but mainly used to increase yield, as
241 precipitation is sufficient for rainfed crops. This means that satellite detection requires the
242 identification of subtle differences between irrigated and rainfed SM. Not surprisingly, this
243 proved a challenge for SMAP as no significant differences were found using the methods
244 presented here.

245 A distinct advantage of microwave detection is that the most direct and observable
246 impact of irrigation is in near-surface SM, the main product from SMAP, in contrast to
247 optical/thermal detection that infers irrigation from surface temperature or other proxies. SMAP
248 and thermal/optical-based products, such as high-resolution, area and time-limited irrigation
249 mapping (e.g., Ozdogan and Gutman, 2008; Ambika et al., 2016) can be used together to
250 evaluate and further develop irrigation physics, triggers, and thresholds in land surface models.
251 SMAP-based detection also creates the possibility of incorporating the irrigation signal into
252 models via DA systems to potentially improve forecasts.

253 As the SMAP record length grows, so too will the ability to mine these data to better
254 understand human impacts on the water cycle. For example, if water conservation methods are
255 widely adopted, how does the SM signal respond? SMAP-based irrigation detection can also be
256 combined with groundwater observations to assist in monitoring agricultural water withdrawals
257 and consumption.

258 **5 Conclusions**

259 This study demonstrated that in three semi-arid regions, SMAP is able to detect the bulk
260 seasonal timing and spatial signature of irrigation via elevated SM relative to non-irrigated
261 adjacent regions. Flood irrigation in the CCV yielded the most dramatic signature and showed
262 SM dynamics consistent with local irrigation practices. In the other two regions, sprinkler
263 irrigation resulted in subtler SM impacts that were often within the range of instrument error,
264 prohibiting the type of intra-seasonal SM analysis that was completed in the CCV. Overall, these
265 results indicate the potential for SMAP, future SM satellite missions, and enhanced products to
266 be used for identifying the timing and location of irrigation. This potential will be more readily
267 achieved with advances in resolution and retrieval over agricultural areas.

268 **Acknowledgments, Samples, and Data**

269 The authors declare no conflicts of interest. This work was supported by NASA grant
270 NNH15ZDA001N-SUSMAP. SMAP data are available via: [https://nsidc.org/data/smap/smap-](https://nsidc.org/data/smap/smap-data.html)
271 [data.html](https://nsidc.org/data/smap/smap-data.html).

272

273

274 **References**

- 275 Alter, R. E., Im, E.-S., & Eltahir, E. A. B. (2015). Rainfall consistently enhanced around the
276 Gezira Scheme in East Africa due to irrigation. *Nat. Geosci*, 8(10), 763–767.
277 doi:10.1038/ngeo2514.
- 278 Ambika, A. K., Wardlow, B., & Mishra, V. (2016). Remotely sensed high resolution irrigated
279 area mapping in India for 2000 to 2015. *Sci. Data*, 3, 160118.
280 doi:10.1038/sdata.2016.118.
- 281 Bonfils, C. & Lobell, D. (2007). Empirical evidence for a recent slowdown in irrigation-induced
282 cooling. *Proc. Natl. Acad. Sci.*, 104(34), 13582–7. doi:10.1073/pnas.0700144104.
- 283 California Rice (2017). How rice grows. California Rice Commission. Retrieved from
284 http://calrice.org/pdf/How_Rice_Grows_final.pdf.
- 285 Colliander, A., et al. (2017). Validation of SMAP surface soil moisture products with core
286 validation sites, *Remote Sens. Environ.*, 191, 214-231. doi:10.1016/j.rse.2017.01.021.
- 287 Entekhabi, D. et al. (2010). The Soil Moisture Active Passive (SMAP) Mission. *Proc. IEEE*, 98,
288 704-716. doi:[10.1109/JPROC.2010.2043918](https://doi.org/10.1109/JPROC.2010.2043918)
- 289 Evans, J. P. & Zaitchik, B. F. (2008). Modeling the large-scale water balance impact of different
290 irrigation systems. *Water Resour. Res.*, 44, W08448. doi:10.1029/2007WR006671.
- 291 Kanamaru, H. & Kanamitsu, M. (2008). Model diagnosis of nighttime minimum temperature
292 warming during summer due to irrigation in the California Central Valley. *J.*
293 *Hydrometeorol.*, 9(5), 1061–1072. doi:10.1175/2008JHM967.1.
- 294 Kumar, S. V., Peters-Lidard, C. D., Santanello, J. A., Reichle, R. H., Draper, C. S., Koster, R. D.,
295 Nearing, G. & Jasinski, M. F. (2015). Evaluating the utility of satellite soil moisture
296 retrievals over irrigated areas and the ability of land data assimilation methods to correct
297 for unmodeled processes. *Hydrol. Earth Syst. Sci.*, 19(11), 4463–4478. doi:10.5194/hess-
298 19-4463-27015.
- 299 Kumar, S. V., Dirmeyer, P. A., Peters-Lidard, C. D., Bindlish, R., & Bolten, J. (2017).
300 Information theoretic evaluation of satellite soil moisture retrievals, *Remote Sens.*
301 *Environ.*, (in press). doi:10.1016/j.rse.2017.10.016.
- 302 Kueppers, L. M., & Snyder, M. (2011). Influence of irrigated agriculture on diurnal surface
303 energy and water fluxes, surface climate, and atmospheric circulation in California. *Clim.*
304 *Dyn.*, 38 (5-6), 1017-1029. doi:10.1007/s00382-011-1123-0.
- 305 Lawston, P. M., Santanello, J. A., Zaitchik, B. F., & Rodell, M. (2015). Impact of irrigation
306 methods on land surface model spinup and initialization of WRF forecasts. *J.*
307 *Hydrometeorol.*, 16 (3), 1135–1154. doi:10.1175/JHM-D-14-0203.1.
- 308 Lawston, P.M., Santanello, J. A., Franz, T. E., & Rodell, M. (2017). Assessment of irrigation
309 physics in a land surface modelling framework using non-traditional and human-practice
310 datasets. *Hydrol. Earth Syst. Sci.*, 21, 2953-2966. doi:10.5194/hess-21-2953-2017.
- 311 Leng, G., Huang, M., Tang, Q., Gao, H., Leung, & L. R. (2014). Modeling the effects of
312 groundwater-fed irrigation on terrestrial hydrology over the conterminous United States.
313 *J. Hydrometeorol.*, 15, 957–972. doi:10.1175/JHM-D-13-049.1.

314 McColl, K. A., Wang, W., Peng, B., Akbar, R., Short Gianotti, D. J., Lu, H., Pan, M., &
315 Entekhabi, D. (2017), Global characterization of surface soil moisture
316 drydowns, *Geophys. Res. Lett.*, *44*, 3682–3690, doi:[10.1002/2017GL072819](https://doi.org/10.1002/2017GL072819).

317 O'Neill, P. E., Chan, S., Njoku, E. G., Jackson, T., & R. Bindlish, R. (2016). SMAP Enhanced
318 L3 Radiometer Global Daily 9 km EASE-Grid Soil Moisture, Version 1.
319 SPL3SMP_E.001. Boulder, Colorado USA. NASA National Snow and Ice Data Center
320 Distributed Active Archive Center. doi: [10.5067/ZRO7EXJ8O3XI](https://doi.org/10.5067/ZRO7EXJ8O3XI). March 20, 2017.

321 Ozdogan, M., and Gutman, G. (2008). A new methodology to map irrigated areas using multi-
322 temporal MODIS and ancillary data: An application example in the continental U.S.,
323 *Remote Sens. Environ.*, *112*, 3520–3537. doi:10.1016/j.rse.2008.04.010.

324 Ozdogan, M., Rodell, M., Beaudoin, H. K., & Toll, D. L. (2010). Simulating the effects of
325 irrigation over the United States in a land surface model based on satellite derived
326 agricultural data, *J. Hydrometeorol.*, *11*, 171–184. doi: [10.1175/2009JHM1116.1](https://doi.org/10.1175/2009JHM1116.1).

327 Pokhrel, Y. N., Hanasaki, N., Wada, Y., Kim, H. (2016). Recent progresses in incorporating
328 human land-water management into global land surface models toward their integration
329 into Earth system models. *Wiley Interdisciplinary Reviews: Water*, *3*(4), 548–574.

330 Puma, M. J. & Cook, B. I. (2010). Effects of irrigation on global climate during the 20th century.
331 *J. Geophys. Res.*, *115*, D16120. doi:10.1029/2010JD014122.

332 Qian, Y., Huang, M., Yang, B. & Berg, L. K. (2013). A modeling study of irrigation effects on
333 surface fluxes and land–air–cloud interactions in the southern Great Plains. *J.*
334 *Hydrometeorol.*, *14*(3), 700–721. doi:10.1175/JHM-D-12-0134.1.

335 Salmon, J. M., Friedl, M. A., Frohling, S., Wisser, D., & Douglas, E. M. (2015). Global rain-fed,
336 irrigated, and paddy croplands: A new high resolution map derived from remote sensing,
337 crop inventories and climate data. *Int. J. Appl. Earth Obs. Geoinf.*, *38*, 321–334.
338 <https://doi.org/10.1016/j.jag.2015.01.014>.

339 Shellito, P. J., Small, E. E., Colliander, A., Bindlish, R., Cosh, M. H., Berg, A. A., Bosch, D. D.,
340 Caldwell, T. G., Goodrich, D. C., McNairn, H., Prueger, J. H., Starks, P. J., van der
341 Velde, R., Walker, & J. P. (2016). SMAP soil moisture drying more rapid than observed
342 in situ following rainfall events, *Geophys. Res. Lett.*, *43*(15). 43, 8068–8075,
343 doi:[10.1002/2016GL069946](https://doi.org/10.1002/2016GL069946).

344 Sorooshian, S., Li, J., Hsu, K. & Gao, X. (2011). How significant is the impact of irrigation on
345 the local hydroclimate in California's Central Valley? Comparison of model results with
346 ground and remote-sensing data. *J. Geophys. Res.*, *116*(D6), D06102.
347 doi:10.1029/2010JD014775.

348 Thenkabail, P. S., Biradar, C. M., Noojipady, P., Dheeravath, V., Li, Y., Velpuri, M., Gumma,
349 M., Gangalakunta, O., Turrai, H., Cai, X., Vithanage, J., Schull, M. A., Dutta, R. (2009).
350 Global irrigated area map (GIAM), derived from remote sensing, for the end of the last
351 millennium. *Internat. J. Remote Sens.*, *30*(14), 3679–3733.
352 doi:10.1080/01431160802698919.

353 USDA National Agricultural Statistics Service Cropland Data Layer (2017). Published crop-
354 specific data layer [Online]. Accessed May 1 2017. USDA-NASS, Washington, DC,
355 available at <https://nassgeodata.gmu.edu/CropScape/>.

356 USDA National Agricultural Statistics Service (2016). *California Crop Weather*. Retrieved from
357 USDA NASS Pacific Field Office. Retrieved from
358 [https://www.nass.usda.gov/Statistics_by_State/California/Publications/Crop_Progress_&](https://www.nass.usda.gov/Statistics_by_State/California/Publications/Crop_Progress_&_Condition/)
359 [_Condition/](https://www.nass.usda.gov/Statistics_by_State/California/Publications/Crop_Progress_&_Condition/)